



Ultrasound and X-ray Cross-Characterization of a Graded Impedance Impactor used for Shock-Ramp Compression Experiments

David Stobbe¹ · James Kelly¹ · Brian Rogers¹ · Kyle Champley¹ · Andrew Townsend¹ · Joseph Tringe¹

Received: 10 February 2023 / Revised: 29 August 2023 / Accepted: 3 October 2023
© The Author(s) 2023

Abstract

In this work we perform ultrasound measurements on an impedance graded impactor made by tape casting magnesium, copper, and tungsten. We also destructively extract small representative samples from the part for complementary characterization with x-ray computed tomography. Combining the two data sets enables direct assignment of some of the measured ultrasound features to specific material characteristics identified by x-ray tomography. Our results demonstrate how ultrasound inspection, informed by x-ray computed tomography, can be used to identify sub-millimeter material amalgamations and spatial heterogeneities in this graded material.

1 Introduction

Progress in advanced manufacturing techniques is providing new types of engineered objects designed at the microscale, with two or more materials [1]. Achievable structures with these methods now include lattice networks with optimized topologies [2] and functionally graded materials with custom metallurgy, microstructure, and material composition [3]. These advanced structures require characterization for quality control, but inspection standards and methods via traditional non-destructive evaluation (NDE) techniques such as x-ray computed tomography (CT), ultrasound testing (UT), or optical interrogation often are not effective due to the novelty and complexity of these material constructions [4–8]. In these cases, new hardware or methods must be developed [9, 10]. Here we demonstrate combining immersion UT and micro- x-ray CT datasets to improve the characterization of a functionally graded

✉ David Stobbe
stobbe2@llnl.gov

¹ Lawrence Livermore National Laboratory, Livermore, CA 94550, USA

material used in shock-ramp compression experiments. Shock compression experiments are an important tool for understanding the physical state and behavior of matter under extreme conditions [11–13]. These experiments are often performed using light gas guns to propel a metal projectile (impactor) up to 8 km/s speeds into a target material, generating a high pressure (>5 Mbars) on the Hugoniot curve and over short times (<1 ns). Using a graded density impactor (GDI), with a customized impedance profile, provides access to a wider range of extreme temperature and pressure states, extends the duration of the experiments, and enables interrogating a continuous set of states during that time instead of a single shocked state on the Hugoniot curve [14–16]. During a shock-ramp compression event, microstructural inhomogeneities extending laterally or into the depth of the impactor, can produce unwanted artifacts in the measured response behavior of the target material. Unfortunately, due to the size and density of most impactors, they cannot be inspected in their entirety using conventional micro- x-ray CT systems (x-ray source does not have sufficient energy to penetrate through the entire object). Scanning immersion ultrasound provides an excellent alternative inspection modality, however, the graded material profile can confound direct assignment of measured ultrasound features to physical defects (challenging to differentiate between voids, material inclusion, anomalies in the impedance profile, etc.). Here we investigate characterizing a magnesium-copper-tungsten GDI using immersion UT informed by a discrete set of micro- x-ray CT measurements taken on portions of the sample that were destructively removed. The overall impedance profile of the GDI is qualitatively evaluated and a microstructural defect is found and quantified using both x-rays and ultrasound.

2 Methods

2.1 GDI

Customized GDIs have been made using tape-casting [17], directed energy deposition [18], and physical vapor deposition [19]. The GDI in this study was made by tape-casting and Fig. 1(a) shows an overview of the manufacturing method. The process generally consists of (1) casting of tapes with varying composition, (2) cutting tape blanks, (3) stacking tapes in a desired compositional sequence, (4) laminating the tapes with pressure and heat, (5) thermally decomposing binders, and (6) hot pressing. Hot-pressed parts are inspected for defects and parts that pass inspection are then machined and assembled into a projectile for launching at a stationary target. The GDI used in this study was approximately 32 mm in diameter and 3.2 mm thick. The expected impedance profile of the GDI can be indirectly determined by combining characterization results from each individual tape layer, this technique is described elsewhere [14, 20]. Here we consider a magnesium-copper-tungsten GDI made from 72 tape layers. The details of each layer are provided in a supplemental table (S1) and the predicted impedance profile of the part used in this study is shown in Fig. 1(b).

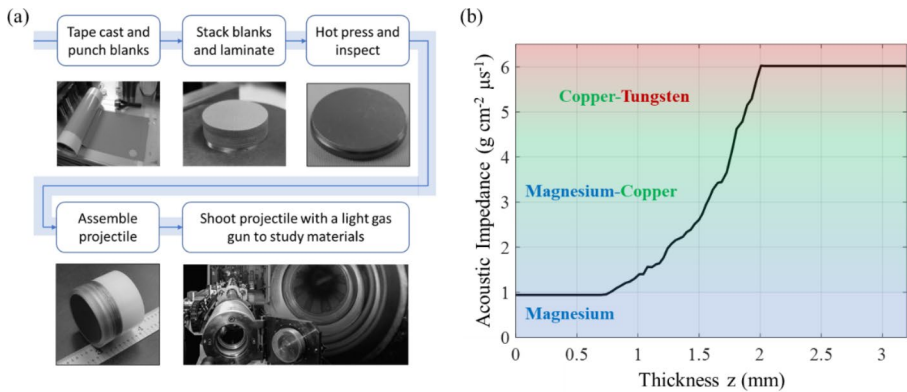


Fig. 1 (a) Fabrication process of graded density impactors (GDI) for use in gas gun shock compression experiments. (b) Impedance profile for GDI predicted by the measured impedance of each individual tape layers

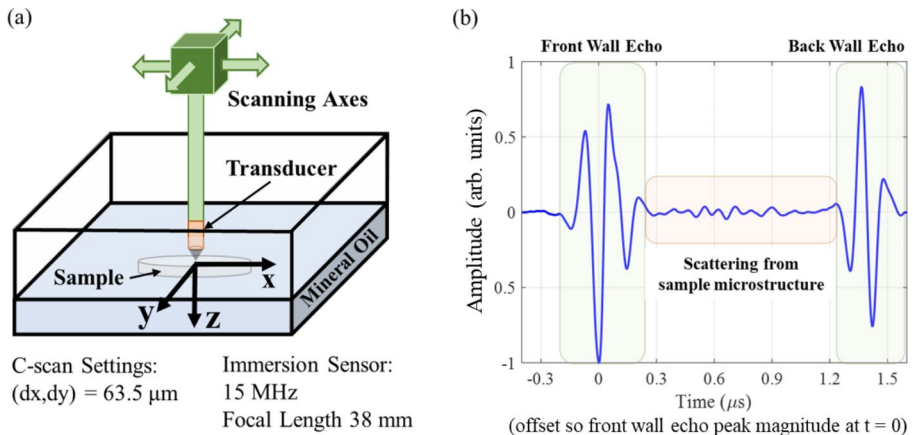


Fig. 2 (a) Schematic of experimental setup for immersion ultrasound scan of GDI. (b) Typical normalized time domain signal (A-scan) measured on GDI where the time is offset so that the front wall echo peak magnitude is at $t=0$. The echo from the front wall and back wall of the sample are identified as well as the scattering from within the sample

2.2 Immersion Ultrasound

The GDI sample was inspected using a commercially available scanning (3-axis) immersion ultrasound system (MISTRAS Group, Inc.), as depicted in Fig. 2(a). A spherically focused immersion sensor with a center frequency of 15 MHz, 9.5 mm aperture, and 38-mm focal length was used. The z -axis was adjusted so that the back wall echo amplitude was maximized, which set the focal point of the beam on the back wall of the sample. The sample was scanned using a unidirectional grid in the x - y plane, where the grid spacing was $63.5 \mu\text{m}$. At each inspection location on the x - y scanning grid, 10 waveforms were averaged, digitally filtered with a bandpass filter

1–25 MHz, digitized at a sampling frequency (SF) of 250 MHz, and recorded as a single amplitude-time trace (A-scan).

An arbitrary A-scan from one measurement location is shown in Fig. 2(b). The A-scan is normalized such that the peak absolute amplitude is unity and is located at time $t=0$. The A-scan consists of two coherent pulses, one from the top, relatively low-impedance surface of the sample (front wall echo) and one from the bottom, relatively high-impedance surface of the sample (back wall echo). In between these two pulses, scattered ultrasound from the interior of the sample is measured. Ultrasound is scattered within the GDI by features such as: tape layer fusion or bonding quality, variation in material phase domains, and grain texture within single material domains. Detecting larger features, like tape layer delamination, can be done by observing standard C-scan images, such as backwall echo amplitude [14].

The total variation from all the individually measured A-scans is shown in Fig. 3. Here the average A-scan is shown along with $\pm 3\sigma$, where σ is the uncorrected sample standard deviation calculated at each point in time using the $N=152,527$ A-scans associated with a 25-mm diameter cylindrical region in the center of the GDI. The outer edges of the sample are excluded as they are machined off prior to assembling into a projectile for using in experiments.

The spatial uniformity of the GDI was interrogated using an absolute deviation (AD) analysis. Every measured A-scan was subtracted from the average A-scan, and then an AD response surface at each measured time step was created with the AD value as the color scale. These images can be viewed sequentially as an AD movie (supplemental video, S2). Examining the AD images at different times is analogous to looking at different depths through the thickness of the GDI. The AD movie reveals three zones within the GDI, each with distinct patterns in the spatial variation. A single representative time/depth from each of these zones is shown in Fig. 4(a–c). The prominent feature in each zone was investigated by destructively removing

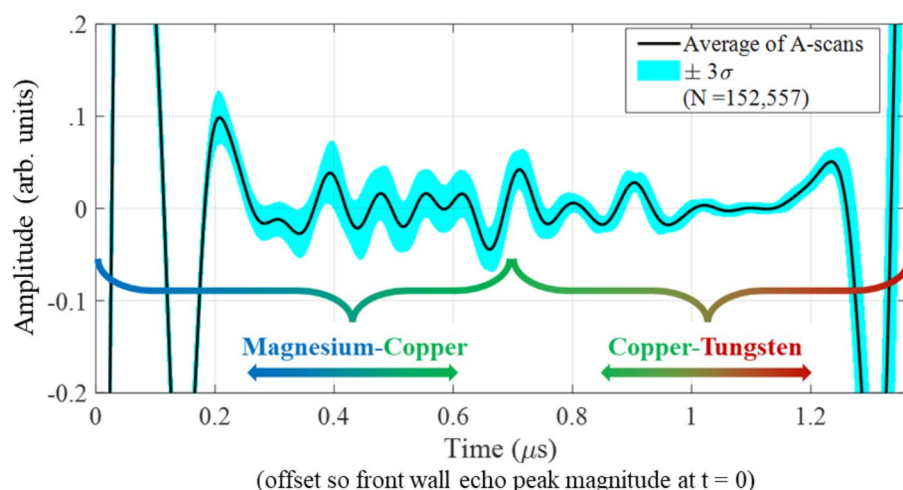


Fig. 3 Average normalized time trace (A-scan) across GDI (black line) and plus/minus three standard deviations at each measured time-step (blue area). The time is offset so that the front wall echo peak magnitude is at $t=0$

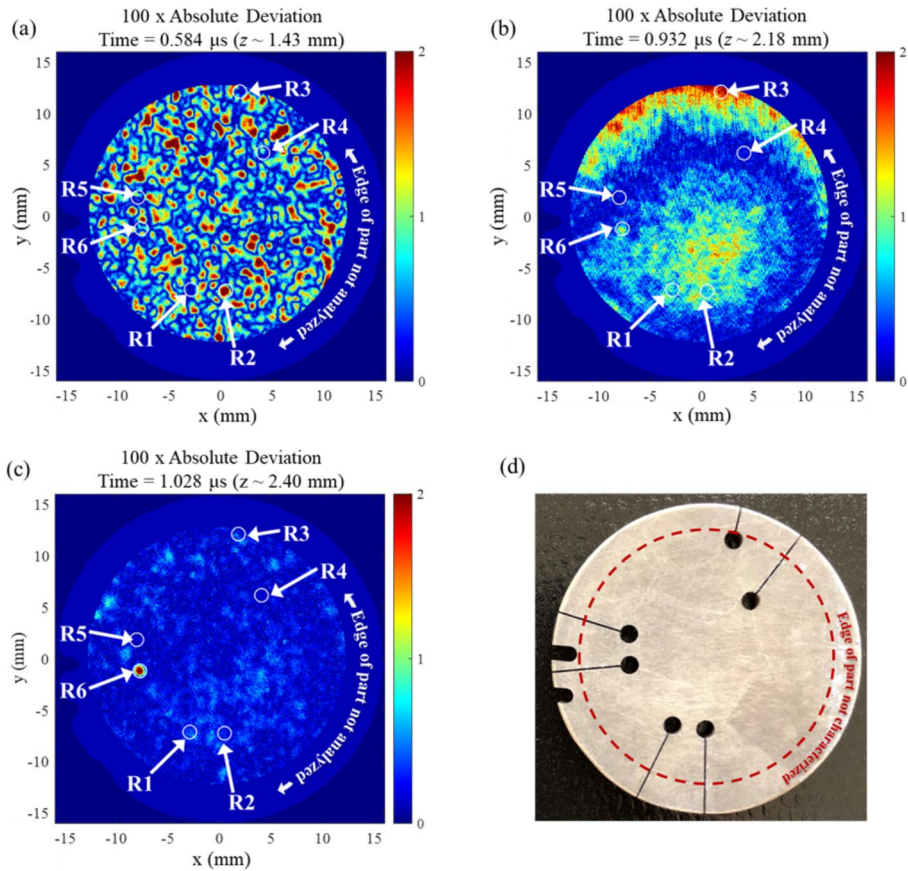


Fig. 4 Absolute deviation from the mean, at each measurement location, in the magnesium-copper portion of the GDI at time=0.584 μ s (a) and in the copper-tungsten portion of the GDI at time=0.932 μ s (b) and time=1.028 μ s (c). The six chosen regions of interest are shown by the white circles and arrows. (d) Photograph of GDI after the 1.5 mm diameter regions of interest were removed by wire electrical discharge machining (EDM)

two 1.5 mm diameter cores for subsequent micro- x-ray CT. Small cores were used since the part is far too large to be x-rayed in its entirety at the resolution required to see the relevant microstructure. In the magnesium-copper portion, the AD exhibits random speckled regions of low and high deviation (e.g., Fig. 4(a)). These regions are irregularly sized and shaped. The locations labeled R1 and R2 were selected as representative of low and high deviation, respectively. In the copper-tungsten impedance ramp portion of the GDI, the AD images (e.g., Fig. 4(b)) show larger continuous regions of high (R3) and low (R4) deviation. In the continuous impedance copper-tungsten region (e.g., Fig. 4(c)), the AD is overall low (R5) except for several localized regions including a very high amplitude region (R6). The six labeled locations were removed from the sample using wire electrical discharge machining (EDM) as shown in Fig. 4(d). Prior to inspection, alignment slots were cut in the edge of the

GDI and used as reference fiducials to locate the regions of interest found in UT in the EDM machine.

2.3 X-ray CT

An x-ray microscope (Xradia 510 Versa, Zeiss) was used to scan the six 1.5-mm diameter cores (R1-R6). For each core, 3,201 transmission radiographs were collected at equally spaced angles as the object was rotated over 360 degrees. The detector exposure time was 13 s at each angle and a 4X objective was positioned in front of the x-ray detector to increase magnification. The x-ray source has a cone beam geometry and was operated at 160 kV and 10 W. The CT volume was reconstructed using cubic voxels with side lengths of 1.66 microns.

Quantitative analysis of the reconstructed CT volumes required correction for scatter, beam hardening, and cone-beam artifacts. Scatter and beam hardening cause a cupping effect where the apparent Linear Attenuation Coefficients (LAC) decrease with depth into the object. The cone-beam artifact causes additional cupping near the bottom and top faces of the cylinder, which occurs because the axial cone-beam CT data provides insufficient information for the reconstruction when there are large gradients in the axial direction. To correct for these effects, reconstruction of the Zeiss CT data was performed using the Livermore Tomography Tools (LTT) software package [21] which uses a multi-material beam hardening algorithm [22]. The cone-beam artifacts were corrected using a method [23] that patches in the missing cone of frequencies based on a model of the GDI's cylindrical shape. The correction algorithms were applied equivalently to each of the six cored samples' x-ray data sets. A cross-sectional image through the center of each core is shown in Fig. 5(a-f). The pure magnesium portion of core R3, $z=0$ to $z\sim 690\text{ }\mu\text{m}$, separated during the EDM machining process and was not inspected, as indicated in Fig. 5(c).

3 Results

The physical causes of the observed deviations in the ultrasound signals are investigated using the x-ray CT data from the six cored locations shown in Fig. 4. The R6 location offers the most straightforward interpretation; the x-ray CT image in Fig. 5(f) shows an approximately cylindrical copper (based on LAC) amalgamation with a diameter and height of $250\text{ }\mu\text{m}$ and $25\text{ }\mu\text{m}$, respectively, located at $z=2.34\text{ mm}$, which is within the constant impedance copper-tungsten region of the GDI. This feature was clearly detected in the UT AD analysis shown in Fig. 4(c). Using the measured wave speeds of the individual tape layers and the time of flight between the front wall echo and the feature, the amalgamation location is calculated to be $z=2.40\text{ mm}$. The variation in location between the UT and CT is likely due to the difference in the actual wave speed through the graded profile versus that derived using individual tape layers, the latter being an indirect method that is subject to process variation. The center of the R6 EDM core was positioned at the center of the feature as measured in the UT scan. The CT results show that the feature is radially centered in the extracted core to within $40\text{ }\mu\text{m}$, thus demonstrating excellent dimensional consistency between the

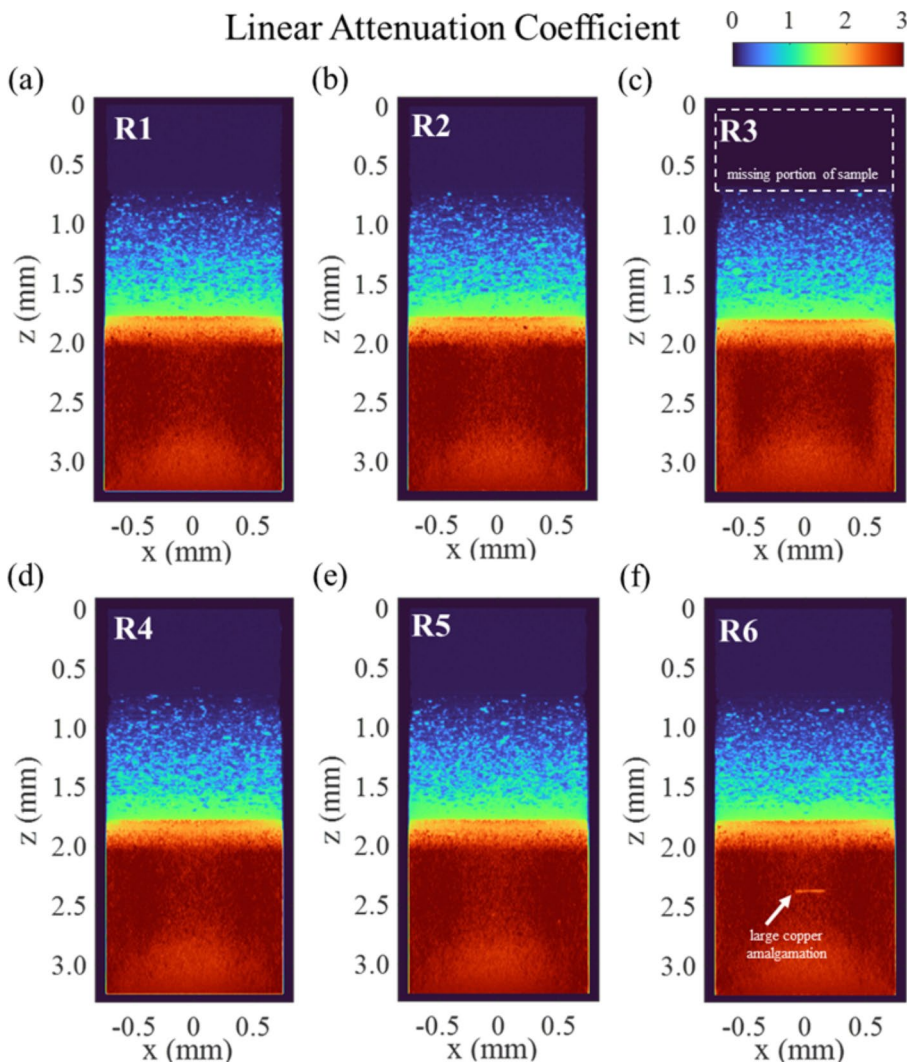


Fig. 5 Cross sectional images of the x-ray computed tomography (CT) for each of the six cylindrical cores removed from the GDI (a–f). The measured linear attenuation coefficient is shown on the color scale

UT and EDM coordinate systems by using the reference notches shown in Fig. 4(d). The UT signal amplitude associated with the R6 amalgamation shown in Fig. 6(a) is beyond the 3σ bands shown in Fig. 3, and this may present an opportunity for automated anomaly detection of similar microstructure features.

Next, the larger continuous AD regions depicted in Fig. 4(b) are investigated using the R3 core. It is hypothesized that the large AD domains shown in Fig. 4(b) are due to spatial variations in the impedance profile (possibly from tape layer sagging during manufacturing). Figure 6(a) shows the average A-scan for each of the six core locations. Each curve is the average of every measured A-scan located within the

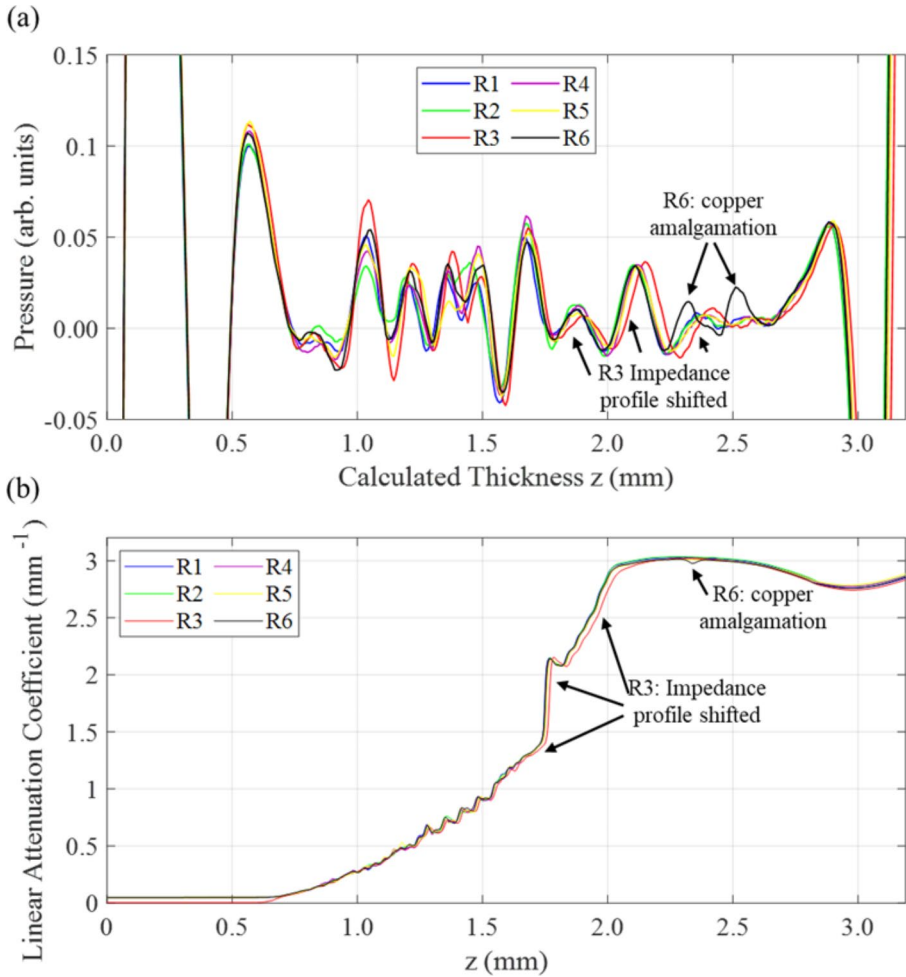


Fig. 6 (a) Average time trace (A-scan) for each of the six regions of interest. The measured longitudinal wave speed for each tape layer is used to convert the x-axis from time to thicknesses. (b) The average linear attenuation coefficient for each of the six regions of interest versus thickness

individual cores. Additionally, the time axis has been converted to thickness (z -axis) using the wave speeds of the individual tape layers. Similarly, Fig. 6(b) shows the average LAC as a function of thickness (z -axis) for each of the cores. Here, the average is taken for every voxel located within a 1-mm diameter cross section instead of the entire 1.5 mm diameter, to avoid potential edge effects [24] which could skew the results. Observing the A-scans in Fig. 6(a), R3 is shifted (delayed) from the other five cores beginning around $z = 1.80$ mm. The same shift in R3 can be observed using the CT LAC results shown in Fig. 6(b). The CT data shows that the R3 core impedance profile lags the other five profiles from about $z = 1.75$ mm to $z = 2.10$ mm. These findings support the proposed spatial heterogeneity of the impedance ramp and the claim that the observed UT response at R3 is caused by this heterogeneity. However, this

analysis should be repeated with multiple core locations within UT regions where it is hypothesized that the impedance ramp has shifted to gain confidence in this interpretation. Figure 6(b) also shows that the axial cone-beam artifacts were not completely removed as evident by the dip in the LAC toward the end GDI, in the constant copper-tungsten region, but is not significant in the graded portion of the microstructure.

Finally, the irregularly shaped and spaced speckled AD features shown in Fig. 4(a) are analyzed using the R2 core. The large AD signal observed in Fig. 4(a) at the R2 location can also be seen in the average A-scans, Fig. 6 (a), at $z \sim 1.4$ mm. At this location the R2 signal greatly deviates from the other five cores. One hypothesis is that the pronounced speckle features are due to heterogeneous scattering from the larger grains and phase domains in the magnesium-copper portion of the GDI, however, the x-ray CT results show similar microstructure and similar average LAC near $z = 1.4$ mm for R1 and R2. Another cause is the use of a focused ultrasound sensor, which causes scatters outside of the focal plane to appear larger and geometrically distorted. The sensor used in this study was focused on the backwall of the sample, which will make this effect larger in the top of the GDI (magnesium-copper portion). However, this does not appear to be the sole cause since the pronounced speckle pattern abruptly stops when the microstructure transitions to copper-tungsten near the middle of the GDI, which is still outside of the focal plane. Additionally, the x-ray CT images show that the material domains are larger in the magnesium-copper portion of the GDI than in the copper-tungsten portion and thus more scattering is expected in the top of the part. Whether or not the current UT inspection technique can provide useful information about microstructure heterogeneity in the magnesium-copper portion of the GDI warrants further investigation. An interesting feature in the LAC plots shown in Fig. 6(b) is consistent cycling behavior between approximately $z = 1.25$ mm and $z = 1.50$ mm. This cyclic behavior is not predicted by the conventional indirect method (Fig. 1(b)) and may be elucidating additional manufacturing defects.

4 Conclusion

This manuscript describes scanning immersion ultrasound measurements of a magnesium-copper-tungsten graded density impactor used for shock-ramp compression experiments. Small portions of interest, based on the ultrasound measurements, were destructively removed from the GDI for micro- x-ray CT characterizations. A sub-millimeter material amalgamation was detected by ultrasound and verified and identified as a copper using micro- x-ray CT. Spatial heterogeneities in the overall impedance ramp profile were also observed in the x-ray CT data and appear to correlate with observed features in the ultrasound measurement. Additional experiments are planned with a designed spatial heterogeneity in the impedance profile to validate the UT approach. Also, we plan on continuing to investigate techniques to assess the homogeneity of the microstructure in the magnesium-copper graded portion of these GDIs.

5 Supplementary Material

See the supplementary material for details and characterization data of the 72 tape layers used to fabricate the GDI, as well as a video where the frames are the measured AD shown sequentially through the thickness of the part.

Supplementary Information The online version contains supplementary material available at <https://doi.org/10.1007/s11220-023-00444-3>.

Acknowledgements Not applicable.

Author Contributions David Stobbe wrote the manuscript, performed the ultrasound measurements and data processing, and generated Figs. 2, 3, 4 and 6. James Kelly assisted with writing the manuscript, oversaw design and manufacturing of the sample, and created Fig. 1. Brian Rogers performed the x-ray inspection and assisted with production of Fig. 5. Kyle Champley performed the computed tomography using the x-ray data and assisted with manuscript writing and Fig. 5. Andrew Townsend conceived the sample fiducials and coordinated the wire EDM of the cores from the sample. Joseph Tringe conceived the project and secured the funding source. All authors assisted with manuscript review and editing. All authors read and approved the final manuscript.

Funding This work was supported by the US DOE LLNL-LDRD 20-SI-001, and performed under the auspices of the U.S. Department of Energy by Lawrence Livermore National Laboratory under Contract DE-AC52-07NA27344.

Data Availability The datasets generated during and analyzed during this study are available from the corresponding author on request.

Declarations

Competing Interests The authors declare no competing interests.

Ethics approval and consent to participate Not applicable.

Consent for publication All materials shown in this paper are owned by the authors and they have given consent for publication.

Open Access This article is licensed under a Creative Commons Attribution 4.0 International License, which permits use, sharing, adaptation, distribution and reproduction in any medium or format, as long as you give appropriate credit to the original author(s) and the source, provide a link to the Creative Commons licence, and indicate if changes were made. The images or other third party material in this article are included in the article's Creative Commons licence, unless indicated otherwise in a credit line to the material. If material is not included in the article's Creative Commons licence and your intended use is not permitted by statutory regulation or exceeds the permitted use, you will need to obtain permission directly from the copyright holder. To view a copy of this licence, visit <http://creativecommons.org/licenses/by/4.0/>.

References

1. Thompson, M., Kathryn, G., Moroni, T., Vaneker, G., Fadel, R., Ian Campbell, I., Gibson, A. (2016). Bernard “Design for Additive Manufacturing: Trends, opportunities, considerations, and constraints.” CIRP annals 65, no. 2 : 737–760.

2. Maconachie, T., Leary, M., Lozanovski, B., Zhang, X., & Qian, M. (2019). Omar Faruque, and Milan Brandt. SLM lattice structures: Properties, performance, applications and challenges. *Materials & Design*, 183, 108137.
3. Loh, G., Hsiang, E., Pei, D., Harrison, & Mario, D. (2018). Monzón. An overview of functionally graded additive manufacturing. *Additive Manufacturing*, 23, 34–44.
4. Echeta, I., Feng, X., Dutton, B., Leach, R., & Piano, S. (2020). Review of defects in lattice structures manufactured by powder bed fusion. *The International Journal of Advanced Manufacturing Technology*, 106(5), 2649–2668.
5. Thompson, A., & Maskery, I. (2016). Leach. X-ray computed tomography for additive manufacturing: A review. *Measurement Science and Technology*, 27(7), 072001.
6. Cerniglia, D., Scafidi, M., Pantano, A., & Rudlin, J. (2015). "Inspection of additive-manufactured layered components " *Ultrasonics* 62 : 292–298.
7. Lopez, A., Bacelar, R., Pires, I., & Santos, T. G. (2018). José Pedro Sousa, and Luísa Quintino. Non-destructive testing application of radiography and ultrasound for wire and arc additive manufacturing. *Additive Manufacturing*, 21, 298–306.
8. Kolb, C. G., Zier, K., Grager, J. C., Bachmann, A., Neuwirth, T., Schmid, S., Haag, M., et al. (2021). An investigation on the suitability of modern nondestructive testing methods for the inspection of specimens manufactured by laser powder bed fusion. *SN Applied Sciences*, 3(7), 1–16.
9. Du Plessis, Anton, I., Yadroitsev, I., Yadroitsava, Stephan, G., & Le Roux (2018). X-ray microcomputed tomography in additive manufacturing: A review of the current technology and applications. *3D Printing and Additive Manufacturing* 5, no. 3 : 227–247.
10. Gillespie, J., Yeoh, W. Y., Zhao, C., Parab, N. D., Tao Sun, A. D., Rollett, B., Lan, & Christopher, M. (2021). Kube. In situ characterization of laser-generated melt pools using synchronized ultrasound and high-speed X-ray imaging. *The Journal of the Acoustical Society of America*, 150(4), 2409–2420.
11. Davison, L. (1979). And Robert Albert Graham "Shock Compression of Solids " *Physics Reports* 55, 4 : 255–379.
12. Kraus, Dominik, A., Ravasio, M., Gauthier, D. O., Gericke, J., Vorberger, S., Frydrych, J., Helfrich (2016). "Nanosecond formation of diamond and lonsdaleite by shock compression of graphite " *Nature communications* 7, 1 : 1–6.
13. Nguyen, J. H., Neil, C., & Holmes (2004). Melting of iron at the physical conditions of the Earth's core. *Nature*, 427(6972), 339–342.
14. Kelly, J. P., Nguyen, J. H., Lind, J., Akin, M. C., Brian, J., Fix, C. K., Saw, E. R., White, W. O., Greene, P. D., & Asimow (2019). Haslam. Application of Al-Cu-W-Ta graded density impactors in dynamic ramp compression experiments. *Journal of Applied Physics*, 125, 14.
15. Krone, R. T., Peter Martin, L., Reed Patterson, J., & Orlikowski, D. (2008). Nguyen. Fabrication and characterization of graded impedance impactors for gas gun experiments from hot-pressed magnesium and polyethylene powders. *Materials Science and Engineering: A*, 479(1–2), 300–305.
16. Ray, A., & Singla, A. (2021). Development of semiempirical equation of state of binary functionally graded materials and its influence on generation of ramp compression: Comparison with bilayer graded density impactors. *Physical Review B*, 103(5), 054301.
17. Martin, L., Peter, D., & Orlikowski (2006). Nguyen. Fabrication and characterization of graded impedance impactors for gas gun experiments from tape cast metal powders. *Materials Science and Engineering: A*, 427, 1–2.
18. Kelly, J. P., Elmer, J. W., Ryerson, F. J., & Lee, J. R. I. (2021). Haslam. Directed energy deposition additive manufacturing of functionally graded Al-W composites. *Additive Manufacturing*, 39, 101845.
19. Brown, J. L., Adams, D. P., Alexander, C. S., & Wise, J. L. (2019). Prime. Estimates of Ta strength at ultrahigh pressures and strain rates using thin-film graded-density impactors. *Physical Review B*, 99(21), 214105.
20. Martin, L., Peter, J. R., Patterson, D., & Orlikowski (2007). Nguyen. Application of tape-cast graded impedance impactors for light-gas gun experiments. *Journal of Applied Physics*, 102(2), 023507.
21. Champley, K. M., Trevor, M., Willey, H., Kim, K., Bond, S. M., Glenn, J. A., Smith, J. S., Kallman, et al. (2022). Livermore tomography tools: Accurate, fast, and flexible software for tomographic science. *NDT & E International*, 126, 102595.
22. Champley, K. M., & Bremer, T. (2014). Efficient and accurate correction of beam hardening artifacts. No. LLNL-CONF-649613. Lawrence Livermore National Lab. (LLNL), Livermore, CA (United States).

23. Leach, W., Lum, J., Champley, K., Azevedo, S., Gardner, C., Kim, H., Stobbe, D., Townsend, A., Joseph, W., & " (2022). *NDT & E International* 127 : 102600.
24. Joseph, P. M., & Spital, R. D. (1981). The exponential edge-gradient effect in x-ray computed tomography. *Physics in Medicine & Biology*, 26(3), 473.

Publisher's Note Springer Nature remains neutral with regard to jurisdictional claims in published maps and institutional affiliations.